

Formation Flight Optimization Using Extremum Seeking Feedback

Paolo Binetti*

Politecnico di Milano, 20159 Milan, Italy

Kartik B. Ariyur[†] and Miroslav Krstić[‡]

University of California, San Diego, La Jolla, California 92093-0411

and

Franco Bernelli[§]

Politecnico di Milano, 20159 Milan, Italy

A comprehensive design procedure based on extremum seeking for minimum power demand formation flight is presented, the first with performance guarantees. The procedure involves the design of a new wake robust formation hold autopilot and transformation of the closed-loop aircraft dynamics to a form in which a newly available rigorous design procedure for extremum seeking is applicable. The design procedure is applied to a formation of Lockheed C-5s, extending the use of maximum performance formation flight to large transports. By the use of available experimental wake data of the C-5, a model of the aircraft in the wake is developed that models aerodynamic interference as feedback nonlinearities. Thus, this work is also the first to attain stable extremum seeking for a plant with nonlinear feedback. Optimal formation flight is attained by online minimization of an easily measurable objective, the pitch angle of the wingman.

I. Introduction

WHEN they fly in formation, two aircraft can achieve a significant reduction in power demand,^{1–3} which can be exploited to improve cruise performance, such as range and speed, or to increase the payload. This more efficient flight condition is attained through aerodynamic interference, by the wingman riding on the upwash field of the leader, like a glider in a thermal. There exists an optimal configuration of the formation that yields maximal reduction in power demand. This configuration can be reached and maintained with dedicated automatic control on the wingman. In fact, at the safe longitudinal separation of two wingspans, maintained between the aircraft (specifically, between the wing of the leader and the wing of the wingman) for collision avoidance,⁴ the effect of aerodynamic interference on the leader is marginal and, in any case, beneficial. (Weak dependence of formation flight benefits on longitudinal separation permits freedom in setting it.³) Thus, to attain maximum-efficiency formation flight, only the wingman needs to be controlled, while the leader can be assumed to be stabilized in straight and level flight by an ordinary autopilot.⁵ The wingman control system is based on a formation-hold autopilot (an autopilot capable of tracking relative position reference signals, that is, wingman–leader separations signals), which is fed an estimate of the optimal separation. The estimate can be calculated from an aerodynamic interference model, or it can be generated by an adaptive feedback control scheme. Both these strategies have been adopted in studies on the problem, which has lately been a focus of intense interest, given the potential payoffs and the availability of enabling avionics and control algorithms.

The model-based open-loop approach has been employed in prior work.^{6–8} Its effectiveness is limited by the uncertainty of aerodynamic interference modeling, accompanied by high sensitivity of power demand reduction to positioning: An error of just 10% of the aircraft wingspan can reduce the benefits by half.⁹ In fact, the need for accurate steady-state performance in the presence of modeling uncertainty calls for adaptive feedback control. This has been done through extremum seeking algorithms.^{3,5} In Ref. 3, a simple discrete time extremum seeking algorithm to maximize aileron deflection was used to attain a power demand reduction of 20% in experimental flight tests of two Dornier aircraft in formation. In Ref. 5, simulation studies of a continuous time extremum seeking algorithm to maximize induced lift were presented. A systematic design procedure was absent in both.

This paper solves problems left open by Refs. 3 and 5 and supplies a generally applicable comprehensive design procedure for minimum power demand formation flight with performance guarantees and easily measurable objective for extremum seeking. This goal is attained through the following steps: 1) modeling of aerodynamic interference as a multiple feedback nonlinearity in the aircraft dynamics, 2) design of a new wake robust formation-hold autopilot, 3) transformation of the closed-loop aircraft dynamics to a form in which a newly available rigorous design procedure for extremum seeking¹⁰ is applicable, and 4) application of the design procedure from Ref. 10 to attain stable extremum seeking, minimizing the pitch angle of the wingman, an easily measurable objective, accounting for wake-induced uncertainties.

We apply the design procedure on a formation of Lockheed C-5s, extending the use of maximum performance formation flight to large transports. We use available experimental wake data of the C-5 to develop a model of the aircraft in the wake that models aerodynamic interference as feedback nonlinearities. Thus, our work is also the first to attain stable extremum seeking for a plant with nonlinear feedback. The choice of the C-5 for study is motivated by the following: Large transports flying long missions, mostly in a cruise condition, can get a high economical payoff from the system; the C-5 has a consistent fleet, which will stay in service for 40 more years with new avionics and engines^{11,12}; and experimental data on the wake of the C-5 are available.¹³

The work is organized as follows: In Sec. II, we model wingman dynamics in the wake of the leader. In Sec. III, we detail design of the new formation-hold autopilot. Section IV is a brief introduction

Received 7 January 2002; revision received 8 May 2002; accepted for publication 19 June 2002. Copyright © 2002 by the authors. Published by the American Institute of Aeronautics and Astronautics, Inc., with permission. Copies of this paper may be made for personal or internal use, on condition that the copier pay the \$10.00 per-copy fee to the Copyright Clearance Center, Inc., 222 Rosewood Drive, Danvers, MA 01923; include the code 0731-5090/03 \$10.00 in correspondence with the CCC.

*Research Assistant, Department of Aerospace Engineering, Via La Masa 34, Member AIAA.

[†]Research Assistant, Department of Mechanical and Aerospace Engineering; kariyur@mae.ucsd.edu.

[‡]Professor, Department of Mechanical and Aerospace Engineering.

[§]Professor, Department of Aerospace Engineering, Via La Masa 34. Senior Member AIAA.

to extremum seeking, the transformation of the optimal formation flight problem to the framework for extremum seeking design,¹⁰ and the extremum seeking design for the C-5s in formation. Section V presents simulations (all simulations performed in MATLAB[®] and SIMULINK) of optimal formation flight of the C-5s in both calm air and in turbulent conditions.

II. Wingman Dynamics in Close Formation Flight

The dynamics of an aircraft in close formation flight is much more complex compared to the dynamics in free flight because of aerodynamic interference (wake-induced forces and moments, which mean new terms in the equations) that arises from the wake generated by other aircraft. Because this formation flight phenomenon significantly alters wingman dynamics, its effects have to be sufficiently captured in modeling for control design, to ensure reliable performance of the control system in the real operating environment.

We solve the problem in four steps. We first develop a model of the wake of the leading C-5 from available wake data,¹³ neglecting influence of the wingman “far behind.” Based on this model, aerodynamic forces and moments on the wingman in the wake of the leader are computed. Then an equilibrium study for the wingman in the wake is performed, yielding powerful insight into the physics of close formation flight benefits. Finally, the dynamics of the wingman in the wake is derived from free flight dynamics.

A. Wake Model

The wake of an aircraft can be described by vortex sheet generation and rollup, rolled-up wake structure, vortex transport, and vortex decay.¹⁴ Two simplifying assumptions can be made immediately, thanks to the value of the longitudinal separation between the aircraft. In fact, the safe two-wingspan figure is large enough for the rollup to be complete, yet small enough to neglect the slow vortex decay process.¹⁵ Vortex transport, which involves a change in orientation and a distortion of the vortex axes from their modeled configuration, is difficult or impossible to predict.¹⁴ This phenomenon translates into uncertainties of the order of 20 ft (Ref. 14) on the optimal separations of the wingman, enough to cut formation flight benefits by 50% (Ref. 9). Hence, we model the rolled-up wake structure as two counter-rotating semi-infinite straight vortices trailing from the wing,¹⁶ parallel to the flight path (with the leader assumed to be in straight and level flight all of the time), and separated by a distance equal to the reduced wing span b_{red} , as shown in Fig. 1, and later design the adaptation to account for the position uncertainty due to vortex transport. For this purpose, the NASA–Burnham–Hallock tangential velocity profile (see Refs. 9, 16) is used because it correlates well with experimental data:

$$V_{\theta}(r) = (\Gamma/2\pi r) \left[r^2 / (r_c^2 + r^2) \right] \quad (1)$$

where V_{θ} is the tangential velocity, Γ is the circulation, r is the radial distance from the vortex axis, and r_c is the core radius of the vortex. The circulation is given by

$$\Gamma = W/\rho V_{\infty} b_{red} \quad (2)$$

and the reduced wingspan by

$$b_{red} = (\pi/4)b \quad (3)$$

where W is the aircraft weight, ρ is the air density, V_{∞} is the reference airspeed, and b is the aircraft wingspan. Finally, based on experimental data,¹³ a 5-ft vortex core radius is estimated for the

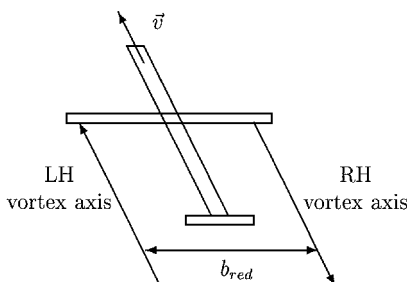


Fig. 1 Aircraft trailing vortices.

C-5 in the high-altitude cruise flight condition. The wake-induced velocity field obtained with this model is given in Appendix A.

B. Forces and Moments on the Wingman in the Wake

When the wake-induced velocity field is used, forces and moments on the wingman in the wake of the leader are calculated, with an emphasis on simple modeling. This choice is crucial, because the alternative is to recalculate the entire straight and level aerodynamic database of the C-5 for flight in the wake, a formidable task.¹⁷

The closeness of aircraft conditions in the wake to trim conditions permits splitting the forces and moments on the aircraft into two terms: a free flight term and an extra term due to flight in the wake. In this subsection we shall only be concerned with the latter, for which some powerful simplifications can be made. First, because the aircraft fly nearly straight and level and parallel, it can be assumed that extra forces and moments depend only on the relative position, that is, separations, between the two aircraft, and on no other states. The relative position x_{rel} and its components, the longitudinal, the lateral, and the vertical separations, respectively, x , y , and z , are defined in Fig. 2.

A second assumption can be made on the same grounds that allow decoupling between longitudinal and lateral-directional dynamics in free flight. It refers to specific forces and moments: The longitudinal and vertical forces and the pitching moment depend only on the upwash distribution, and the lateral force and the yawing moment are only due to the sidewash. No such simplification is possible for the rolling moment, which depends on both the upwash and the sidewash distribution.

To determine the longitudinal and vertical forces, and the pitching moment, we assume that the effect of the upwash distribution is equivalent to that of a uniform distribution obtained by averaging the actual one along the wingspan.⁷ Then we use the available stability derivatives to compute the forces and the moment in one shot. The average upwash \bar{W}_{wake} is given by

$$\bar{W}_{wake}(x, y, z) = \frac{1}{b} \int_0^b W_{wake}(x, y + s, z) c(s) ds \quad (4)$$

where b is the wingspan, W_{wake} is the upwash, $c(s)$ is the chord distribution used as a weight for the average, and s is the lateral coordinate along the wingspan originating at the left wingtip.

The rolling moment due to the upwash, L_{wake} , is calculated using modified strip theory¹⁴:

$$L_{wake}(x, y, z) = -m \frac{1}{2} \rho_0 V_{\infty} a_0 \int_0^b W_{wake}(x, y + s, z) c(s) Q(s) s ds \quad (5)$$

$$Q(s) = \frac{\pi}{4} \sqrt{1 - \left[\frac{2(s - b/2)}{b} \right]^2} \quad (6)$$

$$m = \frac{1}{1 + (2a_0/\pi AR)(1 + \varepsilon)}, \quad \varepsilon = \frac{3TR - 1}{3(1 + TR)} \quad (7)$$

where $Q(s)$ is an elliptical weight, m is a correction factor, a_0 is the two-dimensional lift curve slope, AR is the aspect ratio, and TR is the taper ratio. A value of 5.67 is used for a_0 , as recommended in

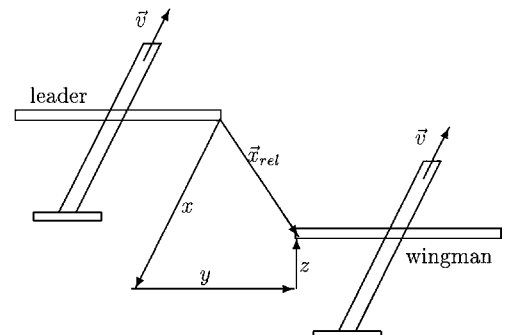


Fig. 2 Configuration of formation flight.

Ref. 14. The rolling moment is given in terms of the rolling moment factor (RMF) = L_{wake}/L_{max} .

Side-force and lateral-directional moments due to the sidewash were calculated assuming a uniform distribution, equal to the value of sidewash at the centerline, V_{wake}^{CL} . We use this simplification because sidewash-induced effects are small compared to other wake effects. The sign convention for V_{wake}^{CL} is opposite to the one for V_{wake} .

With this simple modeling, both the longitudinal dynamics forces and moment and the rolling moment are overestimated (although a more careful choice of the weights can improve accuracy). This, however, shall not be a concern because an overestimate of formation flight benefits leads to conservative design of the control system. More refined modeling, such as vortex lattice,^{9,18} can be used for fine tuning and analysis.

The average upwash \bar{W}_{wake} , the rolling moment L_{wake} , and the sidewash V_{wake}^{CL} fields are shown in Figs. 3–5 as functions of the lateral separation y and of the vertical separation z , at a longitudinal separation $x = 2b$. In fact, there is no significant dependence on the longitudinal separation; hence, a constant value of two wingspans will be used for all aerodynamic interference calculations.

C. Wingman Equilibrium in the Wake

A comparison of horizontal rectilinear flight of the wingman in and out of formation provides an estimate of formation flight benefits and links them to a measurable quantity, which is needed for the adaptive online optimization.

The use of the average upwash concept to model wake-induced forces in the vertical plane, permits proceeding in analogy with flight in uniform rising air. Conclusions can then be reached with simple application of small perturbation theory.

While in the wake, the wingman experiences the leader-induced upwash field, which translates into an increase of the angle of attack and, thus, of lift, unless speed is reduced at the same time. Then,

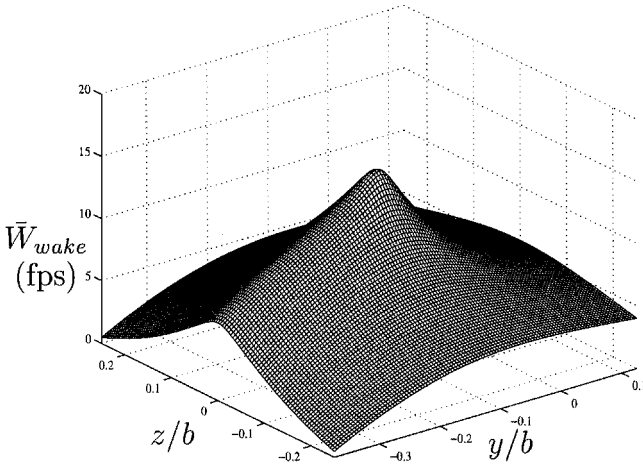


Fig. 3 Average upwash.

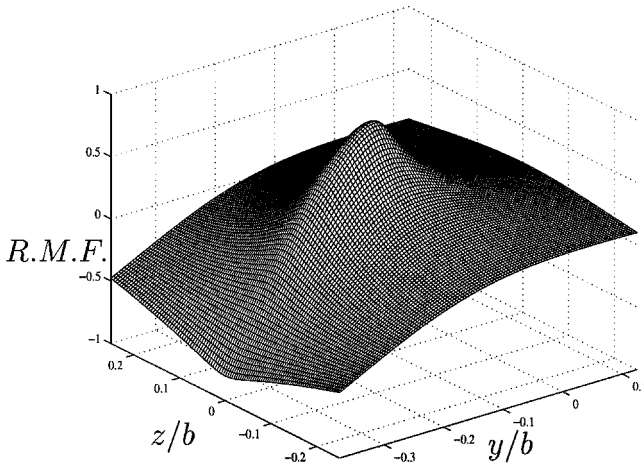


Fig. 4 Rolling moment factor.

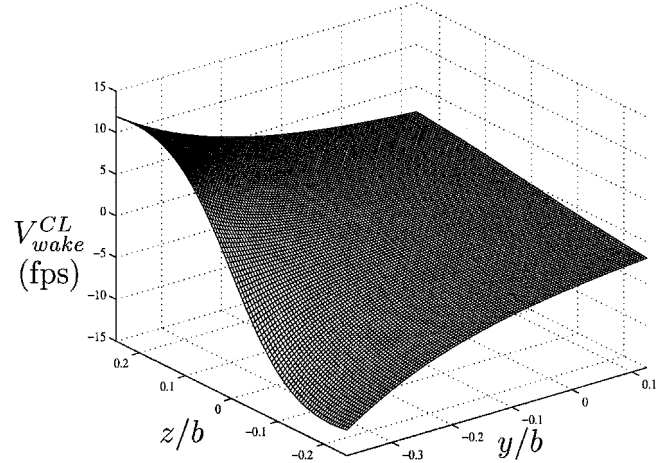


Fig. 5 Sidewash at centerline.

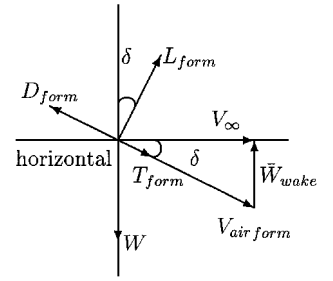


Fig. 6 Forces on wingman in formation.

to maintain vertical equilibrium at the same speed, the wingman has to pitch down. The more pitch down, the more the weight helps thrust balance drag, as shown in Fig. 6, where V_{air} is the airspeed, L is the lift, D is the drag, T is the thrust, and the subscript form refers to steady-state in formation. Hence, thrust reduction, that is, formation flight benefits, are related to the average upwash and to the wingman steady-state pitch angle. The relationship is proportional and specifically

$$\Delta T = T_{form} - T_0 \approx W(\bar{W}_{wake}/V_{\infty}), \quad \bar{\theta} \approx -\delta \approx -57.3\bar{W}_{wake}/V_{\infty} \quad (8)$$

where the subscript 0 refers to steady state out of formation and $\bar{\theta}$ is in degrees. T_0 is 30,000 lb.

These conclusions have two important applications. First, they allow estimation of both the maximum thrust reduction and the relative position at which it is realized, by inspection of the average upwash plot (Fig. 3):

$$\Delta T_{min} = -13,000 \text{ lb}, \quad \Delta T_{\%min} = \Delta T_{min}/T_0 = -43\%$$

$$\bar{\theta}_{min} = -1.13 \quad (9)$$

$$y_{opt} = -24.64 \text{ ft}, \quad z_{opt} = 0 \text{ ft} \quad (10)$$

where the subscript opt refers to the optimal configuration. Second, the pitch angle of the wingman, which can be easily measured, can be fed to the adaptive loop to achieve online optimization.

D. Wingman Dynamics in the Wake

The model is based on standard linearized decoupled dynamics in free flight because state deviations from trim conditions are small. The reference condition chosen for design is cruise at Mach 0.77, 40,000 ft, and 650,000 lb. Dynamics are then given by

$$\dot{\mathbf{x}} = \mathbf{A}\mathbf{x} + \mathbf{B}\mathbf{u}_c \quad (11)$$

where $\mathbf{x} = (\mathbf{x}_{long} \ \mathbf{x}_{lat})^T$ and $\mathbf{u}_c = (\mathbf{u}_{clong} \ \mathbf{u}_{clat})^T$, and $\mathbf{A} = \text{diag}\{A_{long} \ A_{lat}\}$, and $\mathbf{B} = \text{diag}\{B_{long} \ B_{lat}\}$ and where the subscript long stands for longitudinal dynamics and the subscript lat stands for lateral-directional dynamics. The states \mathbf{x}_{long} and \mathbf{x}_{lat} and the control inputs \mathbf{u}_{clong} and \mathbf{u}_{clat} are given in Appendix A; stability derivatives are given in Ref. 19. The dynamics and the saturation points of the

conventional controls of the C-5 have been assumed due to lack of data; they are given in Appendix A. The states can all be measured with accelerometers and gyros, coupled with differential global positioning system (DGPS) and datalink between the two aircraft for separations.²⁰ Beginning 2003, ring-laser gyroscopes and DGPS will be standard equipment on the C-5. The measurement of angle of attack in the highly nonuniform wake-induced velocity field is not meaningful. Hence, its use in feedback should be avoided.

Although perfectly adequate for free flight, linear modeling is not suitable for formation flight. Hence, the dynamics of the wingman in the wake is derived from free flight dynamics, by incorporating formation-related extra forces and moments as feedback nonlinearities (Fig. 7):

$$\dot{\mathbf{x}} = \mathbf{A}\mathbf{x} + \mathbf{B}\mathbf{u}_c + \mathbf{F}\mathbf{u}_{\text{wake}}(y, z) \quad (12)$$

where

$$\mathbf{F} = \begin{pmatrix} F_W & 0 & 0 \\ 0 & F_L & F_V \end{pmatrix} \quad (13)$$

and $\mathbf{u}_{\text{wake}}(y, z) = [\bar{W}_{\text{wake}}(y, z) \ L_{\text{wake}}(y, z) \ V_{\text{wake}}^{\text{CL}}(y, z)]$.

The wake influence matrix \mathbf{F} is given in Appendix A, through its three nonzero partitions, along with the units and the sign conventions for the wake-induced inputs $\mathbf{u}_{\text{wake}}(y, z)$.

III. Formation-Hold Autopilot

The task of the formation-hold autopilot is to drive the wingman to the relative position (with respect to the leader in rectilinear flight) prescribed by the extremum seeking algorithm. This translates into the capability of tracking reference longitudinal, lateral, and vertical separation signals.

The use of the autopilot in an adaptive loop with the purpose of maximum-efficiency flight in an uncertain wake-induced velocity field produces unique design specifications: 1) high-speed tracking in a neighborhood of the optimal configuration to ensure closed-loop stability and speed of convergence with adaptation, 2) ability to track large reference position signals to enable formation join-in

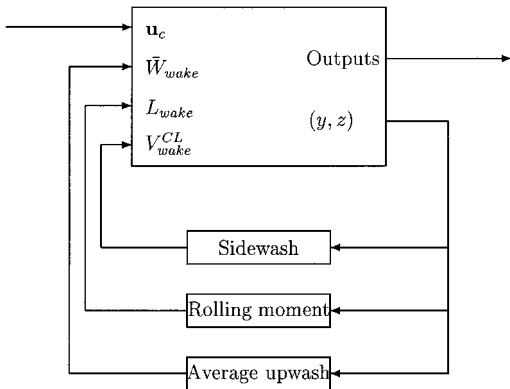


Fig. 7 Wingman in the wake.

from afar, and 3) robustness of tracking performance to aerodynamic interference. (This is crucial to extremum seeking design.)

The uniqueness of these requirements dictate a new design approach, despite the availability of other formation-hold autopilots.^{6–8}

A. Architecture and Design

The structure of the autopilot is shown in Fig. 8. It uses full state measurement (available through an inertial navigation system, a DGPS, and a datalink between the aircraft). It consists of, first, a relative velocities tracking loop (which includes a turn coordination loop based on the sideslip angle β) designed in the error space with the internal model principle²¹ with the feedback gain designed by a linear quadratic regulator (LQR). (This is implemented through the two internal loops in Fig. 8, one proportional to the state and the other proportional to the integral of relative velocities error.) Second, there is a separations tracking loop with classically designed proportional derivative (PD) compensators in the outer loop, along with rate limiters, placed between the inner and the outer loop. High-speed tracking is attained by using high gains; actuator and engine saturation and integrator windup due to large join-in reference signals are prevented by the rate limiters. The following is a compact representation of the closed-loop dynamics in Fig. 8:

$$\dot{\mathbf{x}} = \mathbf{A}\mathbf{x} + \mathbf{B}[(K_{V_{\text{rel}}}/s)(\text{PD}\mathbf{r} - \mathbf{V}_{\text{rel}})] - K_x\mathbf{x} - (K_\beta/s)[\beta] + \mathbf{F}\mathbf{u}_{\text{wake}}(y, z) \quad (14)$$

where $\mathbf{r} = \mathbf{x}_{\text{rel,ref}} - \bar{\mathbf{x}}_{\text{rel}}$, $\bar{\mathbf{x}}_{\text{rel}} = (x \ y \ z)^T$, $\mathbf{V}_{\text{rel}} = (V_x \ V_y \ V_z)^T$, and

$$K_x = \begin{pmatrix} K_{x_{\text{long}}} & 0 \\ 0 & K_{x_{\text{lat}}} \end{pmatrix}, \quad K_{V_{\text{rel}}} = \begin{pmatrix} K_{V_x} & 0 & K_{V_z} \\ 0 & K_{V_y} & 0 \end{pmatrix} \quad (15)$$

$$\text{PD} = \begin{pmatrix} k_{P_x} + k_{D_x}s & 0 & 0 \\ 0 & k_{P_y} + k_{D_y}s & 0 \\ 0 & 0 & k_{P_z} + k_{D_z}s \end{pmatrix} \quad (16)$$

All autopilot parameters are supplied in Appendix B.

B. Robustness to Aerodynamic Interference

This requires that the closed-loop dynamics in Eq. (14) be stable at all points in the wake. Linearizing Eq. (14) about a point (\bar{y}, \bar{z}) in the wake, we get

$$\dot{\mathbf{x}} = \mathbf{A}\mathbf{x} + \mathbf{B} \left[\frac{K_{V_{\text{rel}}}}{s} [(\text{PD}\mathbf{r} - \mathbf{V}_{\text{rel}})] - K_x\mathbf{x} - \frac{K_\beta}{s} [\beta] \right] + \mathbf{F} \frac{\partial \mathbf{u}_{\text{wake}}}{\partial \zeta}(\bar{y}, \bar{z})(\zeta - \bar{\zeta}) \quad (17)$$

where $\zeta = (y, z)$, and $\bar{\zeta} = (\bar{y}, \bar{z})$. The requirement of closed-loop stability at all points (\bar{y}, \bar{z}) in the wake translates to stability of the system in Eq. (17) for a range of gradients $(\partial \mathbf{u}_{\text{wake}}/\partial \zeta)(\bar{y}, \bar{z})$ of the feedback nonlinearity. The structure of Eq. (17) has motivated

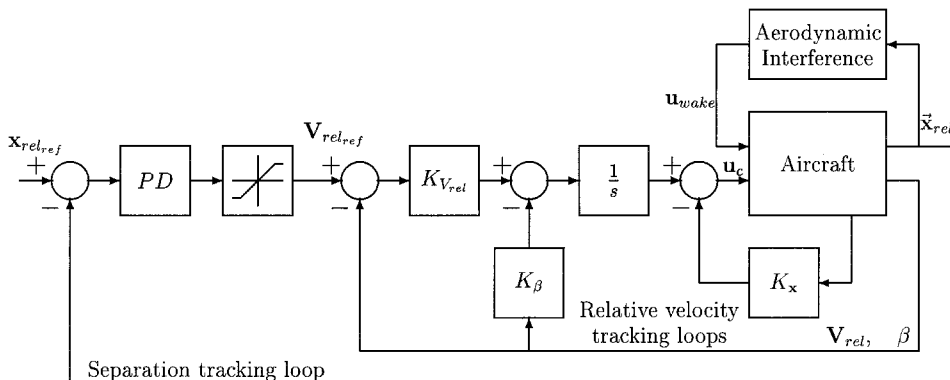


Fig. 8 Formation-hold autopilot.

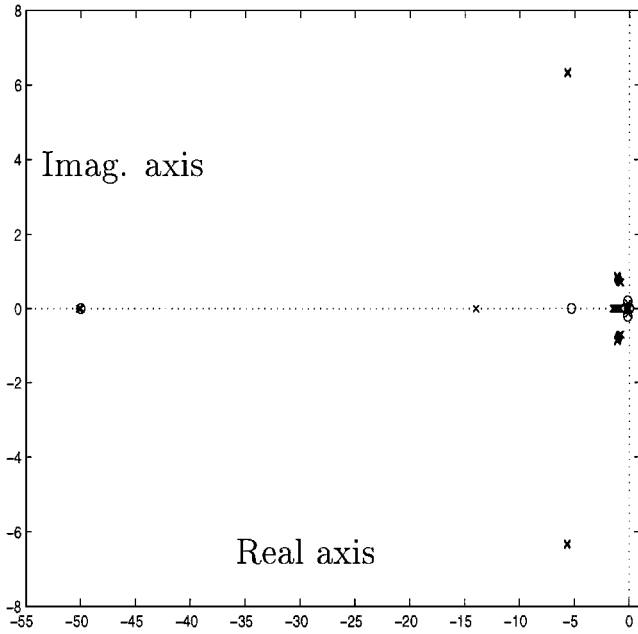


Fig. 9 Autopilot root locus analysis: stability robustness in wake operation.

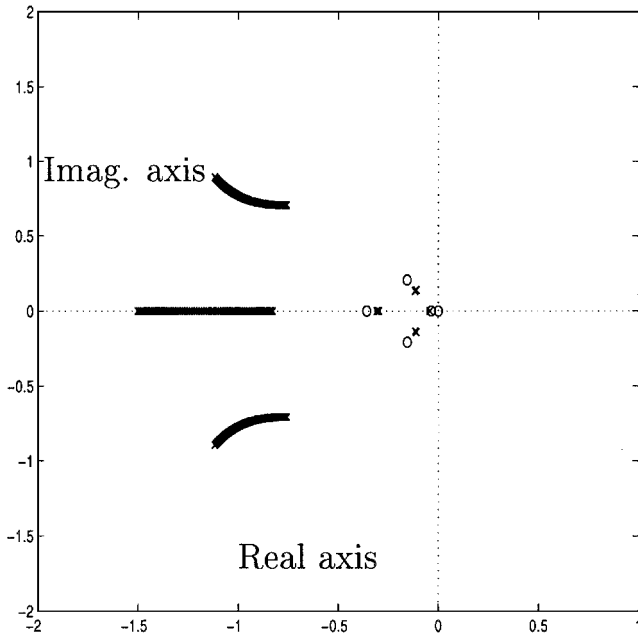


Fig. 10 Autopilot root locus analysis: performance robustness in the wake.

design of high autopilot gains to achieve desired robustness of tracking performance to aerodynamic interference. The stability of the autopilot so designed has been checked by root locus calculations for the range of gradients expected in the wake. As a sample, Fig. 9 shows the root locus of the transfer function between average upwash \bar{W}_{wake} and vertical separation z for the range of gradients in the average upwash field $[-0.345, +0.345]$ (ft/s)/ft. (In Fig. 9, poles are shown with crosses and zeros with circles; some very large zeros in the transfer function are not shown.) Figure 10 presents a zoomed-in version to show that the dominant poles hardly change, resulting in performance practically identical to free flight operation. Robustness to aerodynamic interference is also illustrated by the simulation results to follow.

C. Simulation Results

Figures 11 and 12 show a typical approach to the optimum, assuming perfect knowledge of its position. The wingman is initialized 20 ft below and 20 ft to the right of the optimal position.

Two sets of time histories are shown for comparison: Solid lines represent the autopilot performance with aerodynamic interference, whereas dashed lines represent autopilot performance without aerodynamic interference, which is the condition in which it has been designed. Vertical and lateral separation time histories exhibit almost identical performance with and without aerodynamic interference. The longitudinal separation error is not a concern because it does not have any significant effect on formation flight benefits and because it is well within safety margins for collision avoidance.

Elevator and ailerons deflections reach maximum values almost instantly, to guarantee maximum performance: longitudinal convergence time of 5 s and lateral convergence time of 10 s. Vertical acceleration (not shown) does not exceed a peak of 0.3g and lateral acceleration (not shown) is negligible, thanks to turn coordination. Other simulation runs (not shown to save space) demonstrated good operation of the system starting at any distance from the leader, without reaching actuator saturation. Far away, the rate limiters set vertical approach speed at 500 ft/min and lateral approach speed at 250 ft/min.

As the optimum is reached, thrust is reduced by about 40%, as the aircraft pitches down by about 1 deg, consistently with the equilibrium analysis in Sec. II. The ailerons deflect by about 20 deg, compensating wake-induced rolling moment. Like thrust reduction, this is an overestimate due to the approximate calculation of aerodynamic interference; nonetheless it suggests that high aileron trim drag is to be expected. A method to eliminate it is presented in Sec. V.

IV. Extremum Seeking Control of Formation Flight

The problem of minimizing power demand through formation flight appears to fit intuitively into the framework of extremum seeking control. The choice of objective used in this work (the pitch angle θ), however, does not permit the problem to fit into the standard extremum seeking framework for which a rigorous design method is available. Hence, we transform our problem to fit into the standard framework, and then perform design. We present a brief summary of extremum seeking in Sec. IV.A, the design algorithm in Sec. IV.B, the transformation of our problem to fit the standard scheme in Sec. IV.C, and our design in Sec. IV.D.

A. Extremum Seeking

We introduce the generalized multiparameter extremum seeking scheme in Fig. 13 and sum up the design procedure from Ref. 10. In this scheme, the plant nonlinearity $f(\theta)$ is assumed to be of the form

$$f(\theta) = f^*(t) + [\theta - \theta^*(t)]^T P [\theta - \theta^*(t)] \quad (18)$$

where $P_{l \times l} = P^T > 0$, $\theta = [\theta_1, \dots, \theta_l]^T$, $\theta^*(t) = [\theta_1^*(t), \dots, \theta_l^*(t)]^T$, $\mathcal{L}\{\theta^*(t)\} = \Gamma_\theta(s) = [\lambda_1 \Gamma_{\theta_1}(s), \dots, \lambda_l \Gamma_{\theta_l}(s)]^T$, and $\mathcal{L}\{f^*(t)\} = \lambda_f \Gamma_f(s)$. The purpose of extremum seeking is to make $\theta - \theta^*$ as small as possible, so that the output $F_o(s)[f(\theta)]$ is driven to its extremum $F_o(s)[f^*(t)]$.

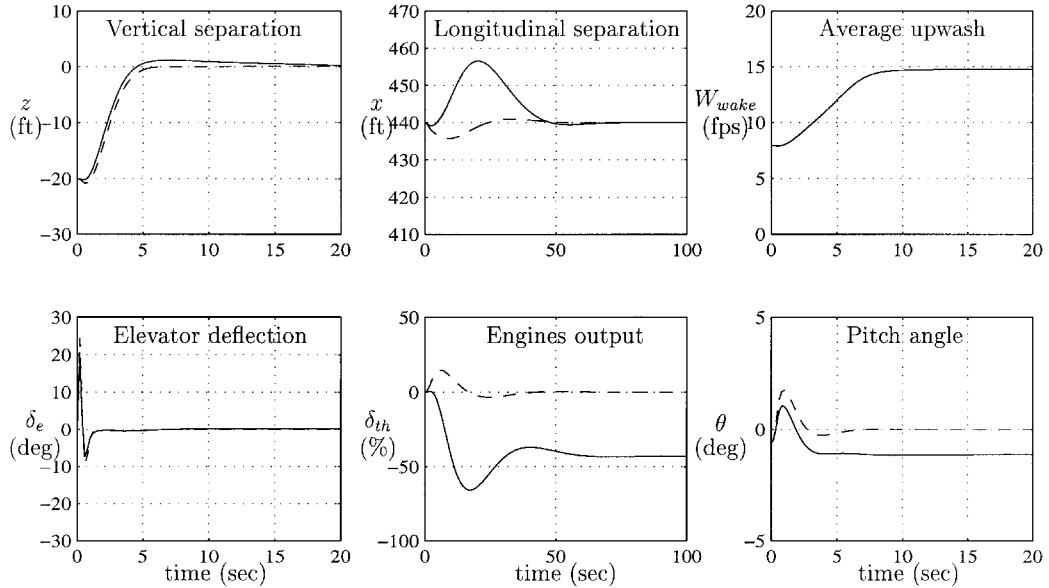
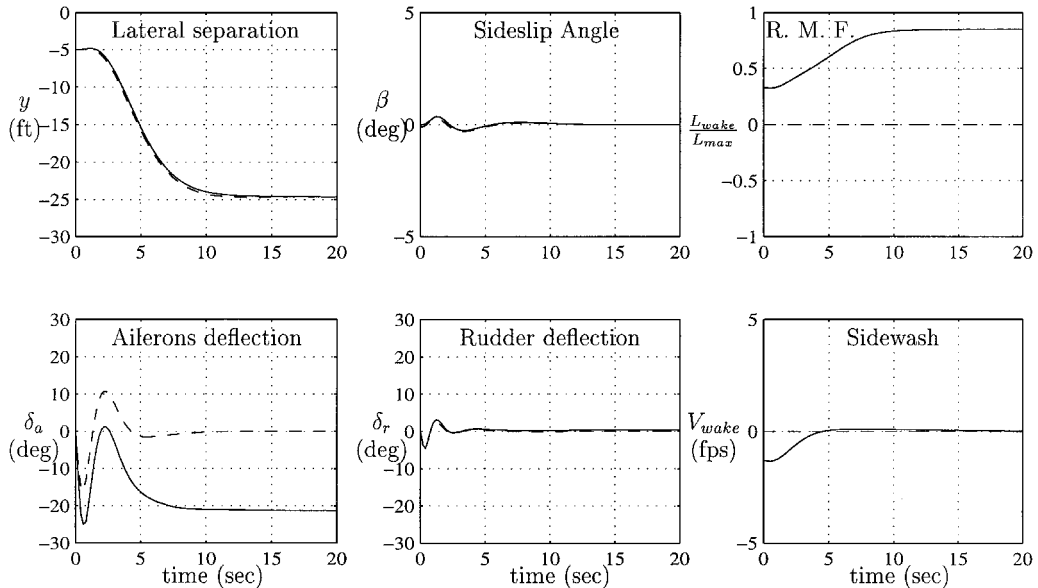
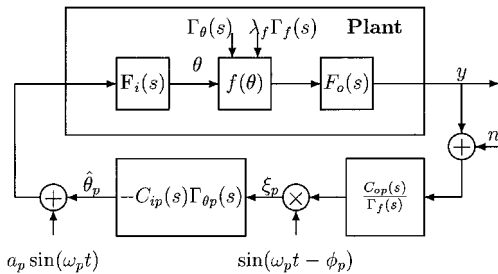
The following assumptions are made for the system in Fig. 13: $F_i(s) = [F_{i1}(s), \dots, F_{il}(s)]^T$ and $F_o(s)$ are asymptotically stable and proper, $\Gamma_\theta(s)$ and $\Gamma_f(s)$ are strictly proper, and $C_{ip}(s)\Gamma_{\theta p}(s)$ and $C_{op}(s)/\Gamma_f(s)$ are proper for all $p = 1, 2, \dots, l$.

Forcing frequencies $\omega_1 < \omega_3 < \dots < \omega_l$ are used in the l parameter tracking loops. The probing signals $a_p \sin \omega_p t$ into the plant help to give a measure of gradient information of the map $f(\theta)$. This is obtained by removing from the output the variation of f^* using the output filter $C_{op}(s)/\Gamma_f(s)$, and then demodulating the signal with $\sin(\omega_p t - \phi_p)$.

Application of the following design algorithm ensures that the output y in Fig. 13 converges exponentially to an

$$\mathcal{O}\left(\frac{1}{\omega_1^2} + l \sum_{p=1}^l a_p^2\right)$$

neighborhood of the extremum $F_o(s)[f^*(t)]$ through Theorem 4.1 in Ref. 10.


Fig. 11 Autopilot performance: longitudinal dynamics.

Fig. 12 Autopilot performance: lateral-directional dynamics.

Fig. 13 Multiparameter extremum seeking with $p = 1, 2, \dots, l$.

B. Design Algorithm

- 1) Select $\omega_1, \omega_2, \dots, \omega_l$ sufficiently large, not equal to frequencies in noise, and with $j\omega_p$ not equal to imaginary axis zeros of $F_{ip}(s)$.
- 2) Set perturbation amplitudes a_p to obtain small steady-state output error \tilde{y} .
- 3) Design each $C_{op}(s)$ asymptotically stable, with zeros that include the zeros of $\Gamma_f(s)$ that are not asymptotically stable and such that $C_{op}(s)/\Gamma_f(s)$ is proper.

4) For each $p = 1, \dots, l$, design $C_{ip}(s)$ such that it does not include poles of $\Gamma_{\theta p}(s)$ that are not asymptotically stable as its zeros, $C_{ip}(s)\Gamma_{\theta p}(s)$ is proper, and $1/\det[\mathbf{I} + \mathbf{X}(s)]$ is asymptotically stable, where $X_{pq}(s)$ denote the elements of $\mathbf{X}(s)$ and

$$X_{pq}(s) = (P_{pq}a_p/2)H_{ip}(s)[e^{j\phi_p}F_{ip}(j\omega_p)H_{op}(s + j\omega_p) + e^{-j\phi_p}F_{ip}(-j\omega_p)H_{op}(s - j\omega_p)] \quad (19)$$

where $H_{ip}(s) = C_{ip}(s)\Gamma_{\theta p}(s)F_{ip}(s)$ and $H_{op}(s) = [C_{op}(s)/\Gamma_f(s)]F_o(s)$. Asymptotic stability of $1/\det[\mathbf{I} + \mathbf{X}(s)]$ may be achieved by designing $C_{ip}(s)$ to minimize $\|X_{pp}/(1 + X_{pp})\|_{H_\infty}$ for each p , using the result in Theorem 5.1 in Ref. 10.

We simplify the design for $C_{ip}(s)$ by setting $\phi_p = -\angle[F_{ip}(j\omega_p)]$ and obtaining $X_{pq}(s) = (a_p P_{pq}/2)|F_{ip}(j\omega_p)||H_{ip}(s)[H_{op}(s + j\omega_p) + H_{op}(s - j\omega_p)]$.

C. Formulation as a Standard Extremum Seeking Problem

We show here that the extremum seeking scheme in Fig. 14 can be transformed to the form in Fig. 13, in which we can then use the available design algorithm. We achieve this objective through the following steps.

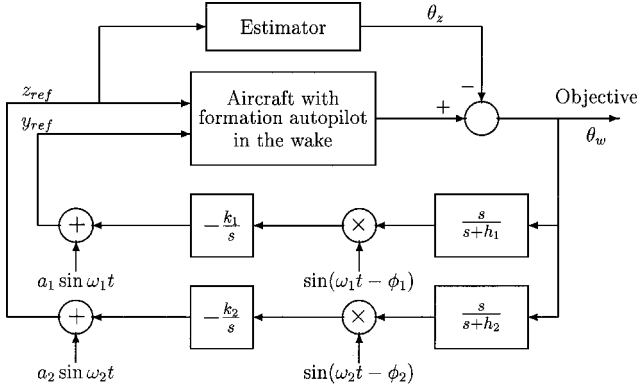


Fig. 14 Extremum seeking for formation flight.

First, write state-space representations of the dynamics from the output of extremum seeking ($y_{\text{ref}}, z_{\text{ref}}$) to the relative position (y, z), and to the pitch angle θ :

$$\begin{aligned} \dot{\mathbf{x}}_{\text{long}} &= (A_{\text{long}} - B_{\text{long}} K_{x_{\text{long}}}) \mathbf{x}_{\text{long}} \\ &+ B_{\text{long}} \left((K_{V_x}/s) \{ (k_{P_x} + k_{D_x} s) [x_{\text{ref}} - x] - V_x \} \right) \\ &+ B_{\text{long}} \left((K_{V_z}/s) \{ (k_{P_z} + k_{D_z} s) [z_{\text{ref}} - z] - V_z \} \right) + F_W \bar{W}_{\text{wake}}(y, z) \\ z &= C_z \mathbf{x}_{\text{long}}, \quad \theta = C_\theta \mathbf{x}_{\text{long}} \end{aligned} \quad (20)$$

$$\begin{aligned} \dot{\mathbf{x}}_{\text{lat}} &= (A_{\text{lat}} - B_{\text{lat}} K_{x_{\text{lat}}}) \mathbf{x}_{\text{lat}} \\ &+ B_{\text{lat}} \left((K_{V_y}/s) \{ (k_{P_y} + k_{D_y} s) [y_{\text{ref}} - y] - V_y \} - (K_{\beta_{\text{lat}}}/s) [\beta] \right) \\ &+ F_L L_{\text{wake}}(y, z) + F_V V_{\text{wake}}^{\text{CL}}(y, z) \\ y &= C_y \mathbf{x}_{\text{lat}} \end{aligned} \quad (21)$$

where

$$K_{\beta_{\text{lat}}} = \begin{pmatrix} K_{\beta_{31}} \\ K_{\beta_{41}} \end{pmatrix}$$

Now, let the transfer functions in free flight (with all wake terms zero) from the reference positions to the position be

$$y(s) = F_{i1}(s) y_{\text{ref}}(s) \quad (22)$$

$$z(s) = F_{i2}(s) z_{\text{ref}}(s) \quad (23)$$

Second, because the autopilot has been designed to be asymptotically stable at all points in the wake, we can write the following transfer function representations from the linearizations of Eqs. (20) and (21) at a point (\bar{y}, \bar{z}) in the wake:

$$\delta y(s) = F_{i1}(s) [1 + \Delta_1(s)] \delta y_{\text{ref}}(s) \quad (24)$$

$$\delta z(s) = F_{i2}(s) [1 + \Delta_2(s)] \delta z_{\text{ref}}(s) \quad (25)$$

where the uncertain transfer functions $\Delta_1(s)$ and $\Delta_2(s)$ arise from the wake feedback nonlinearities.

Third, use the free flight dynamics with the autopilot to estimate the contribution to pitch angle θ_z of the vertical separation reference signal z_{ref} :

$$\begin{aligned} \dot{\hat{\mathbf{x}}}_{\text{long}} &= (A_{\text{long}} - B_{\text{long}} K_{x_{\text{long}}}) \hat{\mathbf{x}}_{\text{long}} \\ &+ B_{\text{long}} \left((K_{V_x}/s) \{ (k_{P_x} + k_{D_x} s) [x_{\text{ref}} - x] - V_x \} \right) \\ &+ B_{\text{long}} \left((K_{V_z}/s) \{ (k_{P_z} + k_{D_z} s) [z_{\text{ref}} - z] - V_z \} \right) \\ \theta_z &= C_\theta \hat{\mathbf{x}}_{\text{long}} \end{aligned} \quad (26)$$

Subtract θ_z from θ to estimate the pitch angle due to the upwash θ_w :

$$\begin{aligned} \dot{\mathbf{e}}_{\text{long}} &= (A_{\text{long}} - B_{\text{long}} K_{x_{\text{long}}}) \mathbf{e}_{\text{long}} + F_W \bar{W}_{\text{wake}}(y, z) \\ \theta_w &= C_\theta \mathbf{e}_{\text{long}} \end{aligned} \quad (27)$$

where $\mathbf{e} = \mathbf{x} - \hat{\mathbf{x}}$. If we define $F_o(s) = C_\theta [s\mathbf{I} - (A_{\text{long}} - B_{\text{long}} K_{x_{\text{long}}})]^{-1} F_W$, the linearization of Eq. (27) at some point (\bar{y}, \bar{z}) in the wake yields $\delta\theta_w = F_o(s) [1 + \Delta_o(s)] \delta z_{\text{ref}}(s)$, where $\Delta_o(s)$ depends on the gradient of the wake field at (\bar{y}, \bar{z}) and $F_o(s) [1 + \Delta_o(s)]$ is exponentially stable at all points in the wake from autopilot design.

Fourth, using that the wake nonlinearities are bounded, we use the following representations for the purpose of extremum seeking design: $y(s) = F_{i1}(s) [y_{\text{ref}}(s) + n_y]$, $z(s) = F_{i2}(s) [z_{\text{ref}}(s) + n_z]$, and $\theta_w(s) = F_o(s) [\bar{W}_{\text{wake}}(y, z)]$. Treatment of the wake terms as bounded noise does not alter performance of the extremum seeking scheme.¹⁰ The finite range of slopes (from 0 to a maximum value) of the wake nonlinearities and the small variation of system poles during motion in the wake due to the high-gain autopilot design ensure that the dynamics are linearly stable at all points in the wake. Moreover, actuator deflections compensate for the wake-induced forces quickly to reach translational equilibrium at each point in the wake. This makes the bounded noise terms very small.

Last, the wake nonlinearity $\bar{W}_{\text{wake}}(y, z)$ maps the outputs of the transfer functions $F_{i1}(s)$ and $F_{i2}(s)$ to the input of $F_o(s)$. Because it has a minimum, it can be represented locally around the minimum in the form in Eq. (18) with piecewise constant θ^* and f^* . Hence, we can write the closed-loop adaptive system in Fig. 14 in the form in Fig. 13 for the purpose of extremum seeking design. An alternative means of transforming the system for design of stable extremum seeking is to analyze directly the closed-loop adaptive system using the method of averaging and modulation properties of the Laplace transform, a lengthy procedure.

Thus, we have a system that satisfies the conditions in Sec. IV.A under which the design algorithm for extremum seeking can be applied. For the purpose of design, we use the transfer functions in free flight as the nominal system and perform extremum seeking design on it in Sec. IV.D, taking into account the wake-induced uncertainty. This is justified because operation in the wake produces only small changes in the closed-loop dynamics with autopilot.

D. Extremum Seeking Design for Formation Flight

We observe that the extremum seeking design for minimum power demand formation flight must, for practical implementation, satisfy the following requirements: achieve stable tracking of the optimal position from afar (at least as much as the uncertainty in vortex position) in the face of wake-induced uncertainty in the transfer functions $\Delta_1(s)$, $\Delta_2(s)$, and $\Delta_o(s)$ and the map second derivative; converge to the extremum fast enough to enable maximal extraction of formation benefits under varying conditions; avoid positioning the wingman far into the downwash region of the leader (where control authority may not be sufficient to stabilize aircraft) by avoiding overshoot in the transient response; and provide reasonable robustness of performance to unexpected atmospheric turbulence.

We design two extremum seeking loops: one for attaining optimal vertical separation and the other for attaining optimal lateral separation between the aircraft. For the process of design, we assume step variations in the optimal separations, that is, $\Gamma_y(s) = \Gamma_z(s) = 1/s$, and in the magnitude of average upwash velocity at the optimal position $\Gamma_{\bar{W}_{\text{wake}}}(s) = 1/s$.

We first apply the design algorithm to the design of the vertical separation optimization loop that sets the reference z_{ref} for the longitudinal aircraft dynamics with autopilot. We choose forcing frequency $\omega_1 = 3$ rad/s (about twice the speed of the dominant poles of the longitudinal dynamics with autopilot) to ensure separation of timescales. Forcing amplitude $a_1 = 0.1/|F_{i1}(j\omega_1)| = 1.22$ ft is chosen so as to achieve an oscillation of 0.1 ft in aircraft vertical separation z . The output compensator is chosen as $C_{o1}(s) = 1/(s + h_1)$ with $h_1 = \omega_1 = 3$ to achieve washout action. The phase of the demodulation signal is chosen as $\phi_1 = -\angle F_{i1}(j\omega_1) = -1.8$ rad. Finally, the input compensator is chosen as a simple gain $C_{i1}(s) = k_1 = 700$.

Next, we apply the design algorithm to the design of the lateral separation optimization loop that sets the reference y_{ref} for the lateral-directional aircraft dynamics with autopilot. We choose forcing frequency $\omega_2 = 1.5$ rad/s (about twice the speed of the dominant poles of the lateral-directional dynamics with autopilot) to ensure separation of timescales. Forcing amplitude

$a_2 = 0.1/|F_{i2}(j\omega_2)| = 1.58$ ft is chosen to achieve an oscillation of 0.1 ft in aircraft lateral separation y . The output compensator is chosen as $C_{o2}(s) = 1/(s + h_2)$ with $h_1 = \omega_2 = 1.5$ to achieve washout action. The phase of the demodulation signal is chosen as $\phi_2 = -\angle F_{i2}(j\omega_2) = 1.45$ rad. Finally, the input compensator is chosen as a simple gain $C_{i2}(s) = k_2 = 175$.

V. Simulation Study

We present here two sets of simulation results showing time trajectories of relative position, extremum seeking objective θ_w and actuator and engine outputs: one in calm air (Fig. 15) and the other showing a brief encounter with clear air turbulence (CAT) (Fig. 16).

For the simulation in calm air, as for the autopilot simulation run, the wingman is initially 20 ft below and 20 ft to the right of the optimal position. (This will in practice be the best available estimate of the optimal position due to the uncertainty introduced by vortex transport.¹⁴) The simulation of the brief encounter with CAT starts in calm air (which is typical because the system would not be used in known turbulent conditions) at the optimal position with turbulence beginning at 40 s.

The states of the longitudinal dynamics, with the exception of the elevator servo states and the engines state, are initialized close to their trim condition in the wake. This initialization, or trimming, is essential for stable functioning of the system because extremum

seeking offers only a local stability guarantee. No such initialization is needed for the lateral-directional dynamics because the objective θ_w is a function of states in the longitudinal dynamics only. The turbulence model includes vertical and lateral gusts with standard Dryden spectrum for CAT at 40,000 ft. Figures 15 and 16 show steady-state values in dashed lines and system performance in solid lines.

The overall result is that engines output is in the neighborhood of steady-state reduction after 80 s, although convergence is complete only after about 120 s. The speed of convergence of the adaptation is ultimately limited by the speed of the aircraft dynamics with autopilot. Here, the gains usable in extremum seeking design are limited by the presence of nonminimum phase zeros in the aircraft dynamics. A possible solution to this problem may be to use direct lift control. The simulation results show several aspects of the design that render practical application of the design procedure in this paper feasible.

1) It is ensured that there is no overshoot in the lateral separation (y) tracking. This is essential to prevent the wingman from entering the downwash region of the leader's wake where roll-control authority may not be sufficient to maintain aircraft position stably.

2) The amplitude of steady-state pitch angle oscillation θ_w is 0.2 deg, which is sufficient for accurate measurement.

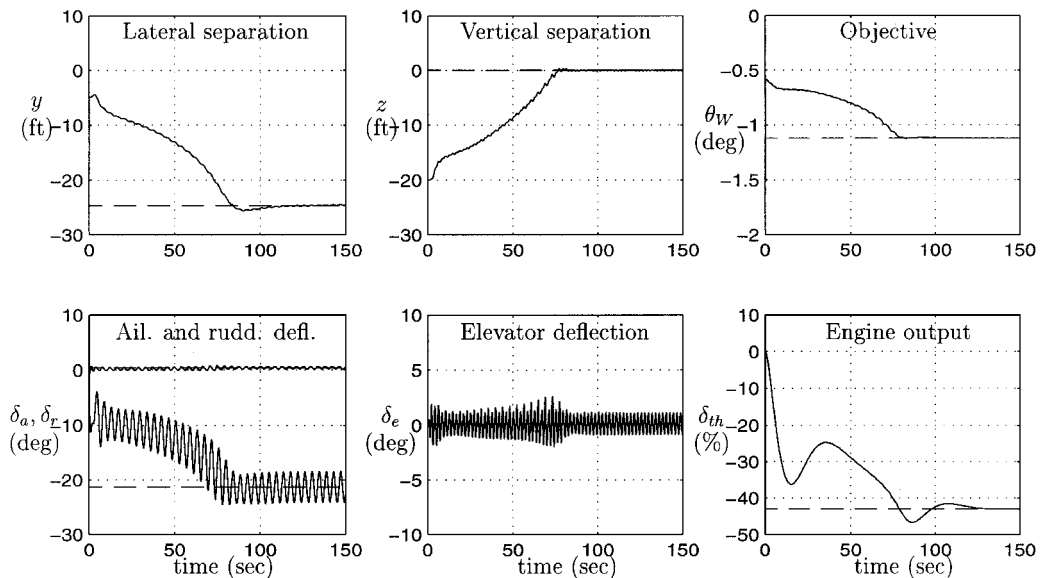


Fig. 15 Extremum seeking performance: calm air.

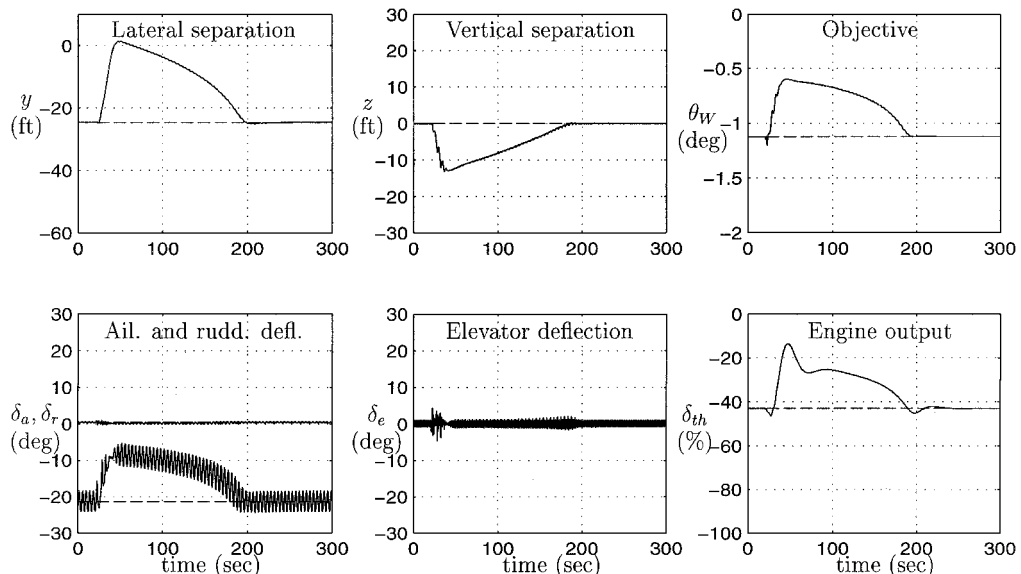


Fig. 16 Extremum seeking performance: brief CAT encounter.

3) Steady-state actuator oscillations are reasonable: Elevator oscillations are about 2 deg at a frequency of 3 rad/s and ailerons and rudder oscillations are, respectively, about 4 and 1 deg at a frequency of 1.5 rad/s. To reduce actuator wear due to the probing signals, extremum seeking can be switched on or off using dead-zone nonlinearities before the extremum seeking integrators depending on the distance from the optimum.

4) Actuators do not hit saturation.

The performance in CAT reveals some fundamental limitations of the extremum seeking method. In fact, the average upwash in the wake has a peak of about 15 ft/s, and the CAT has velocity fluctuations of the order of 10 ft/s. This produces several transient local maxima in the upwash field that mislead the extremum seeking algorithm, which is based essentially on gradient estimation of the upwash field. A practical solution to this problem is switching off the extremum seeking when the vertical acceleration exceeds an acceptable level of $0.2g$. This approach was implemented with the addition of a relay and two switches to the scheme and has been successfully tested in simulation. (The results are not shown here because of space limitations.)

This study did not consider trim drag due to flight in a wake. Aileron trim drag, which is the most persistent, can be balanced by asymmetric fuel loading, more fuel on the left wing tank. If the aircraft has an aft fuel tank, fuel shifting can be applied to cancel elevator trim drag; in any case, this contribution is negligible because the angle-of-attack change from free to formation flight is almost zero. Finally, rudder trim drag can be eliminated using slightly asymmetric thrust.

Our work can be extended to the case of maneuvering flight. The architecture of the lateral-directional part of the autopilot has to be changed, to track the heading reference signals, instead of lateral separation signals. An outer loop has also to be added to this and can be designed as in Ref. 7. The longitudinal part of the autopilot does not need any modification. The extremum seeking algorithm used¹⁰ is capable of tracking general time variations in the location and the value of the maximum upwash velocity. Designs for formations involving more aircraft will need to consider issues of string stability.

VI. Conclusions

We have developed a comprehensive and generally applicable design procedure for minimum power demand formation flight. This has involved modeling aerodynamic interference as a multiple feedback nonlinearity and development of an autopilot robust to operation in the wake that is fast enough to permit stable adaptation (which results in a nonstandard autopilot), as well as extremum seeking design (with stability and performance guarantees) for a system with nonlinear feedback to maximize the pitch down angle of the wingman. Because this work supplies performance and stability guarantees for a robust adaptive solution to the problem of minimum power demand formation flight, making use of an easily measurable optimization objective, it should aid in practical implementation of the concept.

Appendix A: Aircraft Dynamics in Close Formation Flight

A. C-5 and Flight Condition Data

C-5 Galaxy data are listed in Table A1.

Table A1 C-5 Galaxy data

Quantity	Measure
Wingspan b	222 ft, 8 in.
Length l	247 ft, 11 in.
Height h	65 ft, 1 in.
Wing area S	6200 ft ²
Root chord c_R	45 ft, 5 in.
Tip chord c_T	15 ft, 4 in.
Aspect ratio \mathcal{AR}	7.3
Taper ratio TR	0.34
Wing quarter-chord sweep back λ	25 deg
Maximum takeoff weight $W_{TO\max}$	764,500 lb

Table A2 States of wingman dynamics

State	Positive
Ground speed V , kn	Forward
Vertical velocity w , ft/s	Down
Pitch rate q , deg/s	Nose up
Pitch angle θ , deg	Nose up
Longitudinal separation x , ft	Behind leader
Vertical separation z , ft	Above leader
Elevators δ_e , deg	Elevator trailing edge (TE) up
Engines-thrust δ_{th} , deg	More thrust
Lateral velocity v , ft/s	Right wing
Roll rate p , deg/s	Right wing down
Yaw rate r , deg/s	Nose right
Bank angle φ , deg	Right wing down
Heading ψ , deg	Nose right
Lateral separation y , ft	Right of leader
Ailerons δ_a , deg	Right aileron TE up
Rudder δ_r , deg	Rudder TE right

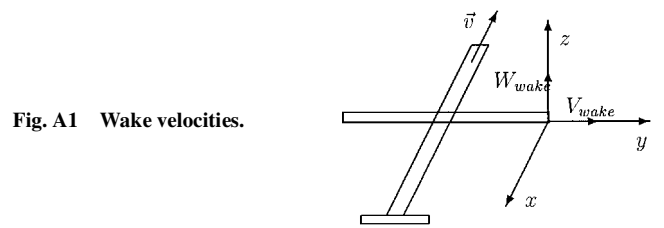


Fig. A1 Wake velocities.

B. Wake-Induced Velocity Field

The wake-induced upwash distribution is

$$W_{\text{wake}}(x, y, z) = W_R(x, y, z) + W_L(x, y, z) \quad (\text{A1})$$

where

$$W_R(x, y, z) = \frac{\Gamma}{4\pi} \frac{y}{y^2 + z^2 + r_c^2} \left(1 + \frac{x}{\sqrt{x^2 + y^2 + z^2}} \right) \quad (\text{A2})$$

$$W_L(x, y, z) = \frac{\Gamma}{4\pi} \frac{y + b}{(y + b)^2 + z^2 + r_c^2} \left(1 + \frac{x}{\sqrt{x^2 + (y + b)^2 + z^2}} \right) \quad (\text{A3})$$

are the contributions, respectively, from the right and from the left trailing vortex.

The wake-induced sidewash distribution is

$$V_{\text{wake}}(x, y, z) = V_R(x, y, z) + V_L(x, y, z) \quad (\text{A4})$$

where

$$V_R(x, y, z) = (\Gamma/4\pi) \left[z / (y^2 + z^2 + r_c^2) \right] \left(1 + x / \sqrt{x^2 + y^2 + z^2} \right) \quad (\text{A5})$$

$$V_L(x, y, z) = (\Gamma/4\pi) \left\{ z / \left[(y + b)^2 + z^2 + r_c^2 \right] \right\} \times \left[1 + x / \sqrt{x^2 + (y + b)^2 + z^2} \right] \quad (\text{A6})$$

are the contributions, respectively, from the right and from the left trailing vortex. Figure A1 shows the origin of the coordinate system at the right wingtip of the leader and the directions of the upwash W_{wake} and sidewash V_{wake} .

C. Free Flight Model Data

Tables A2–A4 give the states ($\mathbf{x}_{\text{long}, 8 \times 1}$, $\mathbf{x}_{\text{lat}, 8 \times 1}$) and the inputs of the model, as well as the parameters of the actuators. All quantities are to be intended as perturbations from their value at the reference

Table A3 Inputs of wingman dynamics

Input: u_{clong}	Positive
Elevators command δ_{e_c} , deg	Elevator TE up
Thrust command δ_{th_c} , deg	More thrust
Ailerons command δ_{a_c} , deg	Right aileron TE up
Rudder command δ_{r_c} , deg	Rudder TE right
Average upwash \bar{W}_{wake} , ft/s	Upward
Rolling moment L_{wake} , lb · ft	Right wing down
Sidewash V_{wake}^{CL} , ft/s	To the left

Table A4 Actuation: (first-order lags) dynamics and saturations

Control	(Pole) frequency	Saturation
δ_e	10 rad/s	+25/-25 deg
δ_{th}	0.2 rad/s	+10,000/-30,000 lb
δ_a	10 rad/s	+25/-25 deg
δ_r	10 rad/s	+25/-25 deg

condition for which linearization is performed, the exception being the separations, x , y , and z . For free flight,

$$k_{D_x} = 0.025, \quad k_{D_y} = 0, \quad k_{D_z} = 0 \quad (B2)$$

and by rate limiters,

$$|V_x|_{\max} = 4 \text{ kn}, \quad |V_y|_{\max} = 250 \text{ ft/min}, \quad |V_z|_{\max} = 500 \text{ ft/min} \quad (B3)$$

The state-space relative-velocities-tracking part of the autopilot is made up by state-proportional gain matrices:

$$K_{x_{long}} = \begin{pmatrix} -57.0 & -909 & 50.1 & 1090 & 0 & 0 & 1.74 & -0.0297 \\ 20400 & -8010 & 411 & 17900 & 0 & 0 & -0.0595 & 1.82 \end{pmatrix} \quad (B4)$$

$$K_{x_{lat}} = \begin{pmatrix} 629 & 12.3 & 24.7 & -9.39 & 654 & 0 & 0.362 & 0.0540 \\ 289 & 1.76 & 29.2 & -10.4 & 341 & 0 & 0.0540 & 0.557 \end{pmatrix} \quad (B5)$$

and by the integrative part whose gain matrices are given by

$$A_{long} = \begin{pmatrix} -0.00380 & 0.0180 & -0.470 & -0.332 & 0 & 0 & -0.0103 & 0.0000291 \\ -0.102 & -0.427 & 13.0 & -0.0343 & 0 & 0 & 0.286 & 0.00000172 \\ -0.0214 & -0.0963 & -0.645 & 0.000367 & 0 & 0 & 0.938 & 0.00000816 \\ 0 & 0 & 1.00 & 0 & 0 & 0 & 0 & 0 \\ 1.69 & 0 & 0 & 0 & 0 & 0 & 0 & 0 \\ 0 & -0.998 & 0 & 13.0 & 0 & 0 & 0 & 0 \\ 0 & 0 & 0 & 0 & 0 & 0 & -10.0 & 0 \\ 0 & 0 & 0 & 0 & 0 & 0 & 0 & -0.200 \end{pmatrix} \quad (A7)$$

$$B_{long} = \begin{pmatrix} 0 & 0 & 0 & 0 & 0 & 0 & 10.0 & 0 \\ 0 & 0 & 0 & 0 & 0 & 0 & 0 & 0.200 \end{pmatrix}^T \quad (A8)$$

$$A_{lat} = \begin{pmatrix} -0.0636 & 0.794 & -13.0 & 0.561 & 0 & 0 & -0.000679 & -0.118 \\ -0.0831 & -0.706 & 0.233 & 0 & 0 & 0 & 0.298 & -0.112 \\ 0.0182 & -0.0776 & -0.0991 & 0 & 0 & 0 & 0.00618 & 0.324 \\ 0 & 1 & 0.0612 & 0 & 0 & 0 & 0 & 0 \\ 0 & 0 & 1.00 & 0 & 0 & 0 & 0 & 0 \\ 1.00 & 0 & 0 & -0.794 & 13.0 & 0 & 0 & 0 \\ 0 & 0 & 0 & 0 & 0 & 0 & -10.0 & 0 \\ 0 & 0 & 0 & 0 & 0 & 0 & 0 & -10.0 \end{pmatrix} \quad (A9)$$

$$B_{lat} = \begin{pmatrix} 0 & 0 & 0 & 0 & 0 & 0 & 10.0 & 0 \\ 0 & 0 & 0 & 0 & 0 & 0 & 0 & 10.0 \end{pmatrix}^T \quad (A10)$$

D. Formation Flight Model: Influence Matrices

$$F_W = (0.0180 \quad -0.428 \quad -0.0965 \quad 0 \quad 0 \quad 0 \quad 0 \quad 0)^T \quad (A11)$$

$$F_L = (0 \quad 0.00000206 \quad 0 \quad 0 \quad 0 \quad 0 \quad 0 \quad 0)^T \quad (A12)$$

$$F_V = (-0.0636 \quad -0.0831 \quad -0.0182 \quad 0 \quad 0 \quad 0 \quad 0 \quad 0)^T \quad (A13)$$

Appendix B: Formation-Hold Autopilot Parameters

The classical separations-tracking part of the autopilot is made up by PD compensators,

$$k_{p_x} = 0.030, \quad k_{p_y} = 12, \quad k_{p_z} = 25 \quad (B1)$$

$$K_{V_x} = \begin{pmatrix} 15.6 \\ -2180 \end{pmatrix}, \quad K_{V_z} = \begin{pmatrix} -1.38 \\ -9.88 \end{pmatrix} \quad (B6)$$

$$K_{V_y} = \begin{pmatrix} -0.403 \\ -0.193 \end{pmatrix}, \quad K_{\beta} = \begin{pmatrix} -13.6 \\ -28.5 \end{pmatrix} \quad (B7)$$

Acknowledgments

This work was supported in part by grants from the Air Force Office of Scientific Research, the Office of Naval Research, and the National Science Foundation.

References

- ¹Cutts, C. J., and Speakman, J. R., "Energy Savings in Formation Flight of Pink-Footed Geese," *Journal of Experimental Biology*, Vol. 189, 1994, pp. 251–261.
- ²Chichka, D. F., and Speyer, J., "Solar-Powered, Formation-Enhanced Aerial Vehicle Systems for Sustained Endurance," *Proceedings of the 1998 American Control Conference*, American Automatic Control Council, Evanston, IL, 1998, pp. 684–688.
- ³Hummel, D., "The Use of Aircraft Wakes to Achieve Power Reduction in Formation Flight," *Proceedings of the Fluid Dynamics Panel Symposium*, AGARD, 1996, pp. 1777–1794.
- ⁴Myatt, J. H., and Blake, W. B., "Aerodynamic Database Issues for Modeling Close Formation Flight," AIAA Paper 99-4194, Aug. 1999.
- ⁵Chichka, D. F., Speyer, J., and Park, C. G., "Peak-Seeking Control with Application to Formation Flight," *Proceedings of the 38th IEEE Conference on Decision and Control*, IEEE Publications, Piscataway, NJ, 1999, pp. 2463–2470.
- ⁶Giulietti, F., Pollini, L., and Innocenti, M., "Autonomous Formation Flight," *IEEE Controls Systems Magazine*, Vol. 20, No. 6, 2000, pp. 34–44.
- ⁷Pachter, M., D'Azzo, J. J., and Proud, A. W., "Tight Formation Flight Control," *Journal of Guidance, Control, and Dynamics*, Vol. 24, No. 2, 2001, pp. 246–254.
- ⁸Schumacher, C., and Singh, S., "Nonlinear Control of Multiple UAVs in Closed Coupled Formation Flight," AIAA Paper 2000-4373, Aug. 2000.
- ⁹Blake, W. B., and Multhopp, D., "Design Performance and Modeling Considerations for Closed Formation Flight," AIAA Paper 98-4343, Aug. 1998.
- ¹⁰Ariyur, K. B., and Krstic, M., "Analysis and Design of Multivariable Extremum Seeking," *Proceedings of the 2002 American Control Conference*, American Automatic Control Council, Evanston, IL, pp. 2903–2908.
- ¹¹Kandebo, S. W., "C-5 Reengining Should Boost Performance," *Aviation Week and Space Technology*, Vol. 153, No. 7, 14 Aug. 2000, pp. 26, 27.
- ¹²Ramsey, J., "C-5 Modernization—Step by Step," *Avionics Magazine*, Vol. 24, No. 8, 2000, pp. 30–34.
- ¹³Garodz, L. J., "Measurement of the Wake Characteristics of The Boeing 747, Lockheed C-5A, and Other Aircraft," NASA, Project 177-621-03X (Special Task 1), National Aviation Facilities Experimental Center, Atlantic City, NJ, April 1970.
- ¹⁴Hallock, J. N., and Eberle, W. R., "Aircraft Wake Vortices: A State of the Art Review of the United States R&D Program," Transportation Systems Center, Dept. of Transportation, Rept. DOT-TSC-FAA-77-4, Cambridge, MA, Feb. 1977.
- ¹⁵Scheiman, J., Megrail, J. L., and Shivers, J. P., "Exploratory Investigation of Factors Affecting the Wing Tip Vortex," NASA Langley Research Center, TM X-2516, Hampton, VA, April 1972.
- ¹⁶Hallock, J. N., "Aircraft Wake Vortices: An Assessment of the Current Situation," Transportation Systems Center, Research and Special Programs Administration, Dept. of Transportation, Rept. DOT-TSC-FAA-90-6, Cambridge, MA, Jan. 1991.
- ¹⁷Blake, W. B., "Aerodynamic Model for Simulation of Closed Formation Flight," AIAA Paper 2000-4034, Aug. 2000.
- ¹⁸Maskew, B., "Formation Flying Benefits Based on Vortex Lattice Calculations," Analytical Methods, Inc., Rept. CR-151974, Bellevue, WA, 1977.
- ¹⁹Heffley, R. K., and Jewell, W. F., "Aircraft Handling Qualities Data," Systems Technology, Inc., Rept. CR-2144, Washington, DC, Dec. 1972.
- ²⁰Williamson, W., Min, J., Speyer, J. L., and Farrell, J., "A Comparison of State Space, Range Space, and Carrier Phase Differential GPS/INS Relative Navigation," *Proceedings of the 2000 American Control Conference*, American Automatic Control Council, Evanston, IL, 2000, pp. 2932–2938.
- ²¹Franklin, G. F., Powell, J. D., and Emami-Naeini, A., "Integral Control and Robust Tracking," *Feedback Control of Dynamic Systems*, 3rd ed., Addison Wesley Longman, Reading, MA, 1995, pp. 551–560.